Modeling Microwave and Hybrid Heating Processes Including Heat Radiation Effects

Jens Haala, *Member, IEEE,* and Werner Wiesbeck, *Fellow, IEEE*

***Abstract*—This paper presents an efficient simulation tool for conventional, microwave, and combined heating. Two heat-transfer mechanisms are included: conductive and radiant heat transfer. The conductive heat transfer is modeled by a finite-difference algorithm. A modeling technique for radiant heat transfer in nonuniform grids has been developed and is here presented for the first time. For the radiant heat transfer a finite-difference scheme is not applicable, as radiation from a material surface is not bounded to the immediate vicinity, as is conductive heat transfer. Therefore, ray optical methods are used. Rays connecting mutually visible surfaces are obtained by a new fast method. Necessary, but acceptable simplifications allow fast computations. The algorithms are integrated conveniently together with an electromagnetic finite-difference time-domain program to one simulation tool. Representative simulations are presented for an oven heated conventionally, by microwaves, and by a combination of both.**

***Index Terms*—FDTD, heat radiation, microwave heating.**

I. INTRODUCTION

THERMAL modeling is mandatory for the optimization of heating processes in ovens. Especially in combination with microwaves, the heating process has to be carefully designed to achieve a fast and uniform heating. Various reports [1]–[10] reported electromagnetic-field computations of microwave ovens, but only few authors [11], [12] include a thermal model in their procedures. To the authors' knowledge, all models consider only heat transfer by conduction, while radiation is usually neglected. This simplification becomes questionable at higher temperatures. In fact, with increasing temperature, radiant heat exchange becomes more and more important since the energy emitted from a material surface increases proportional to T^4. In contrast, energy transported by heat conduction is only proportional to T. Radiant heat transfer eventually prevails over conductive heat transfer. This paper specifically includes radiant heat transfer and, therefore, closes the gap of neglected radiant heat exchange.

Pure thermal problems are mostly simulated by finite-element modeling, some of which include radiation. Heating by microwaves is sometimes considered, but the variation of the electromagnetic field with increasing temperature due to changing material properties is not. Additionally, these models normally perform only steady-state calculations.

For the optimization of ovens, one needs to determine the dynamic heat process. Hence, a combination of thermal and electromagnetic simulations must be used. Both radiation and the influence of increasing temperature on the electromagnetic field must be considered.

The finite-difference time-domain (FDTD) method has proven to be an excellent algorithm for the calculation of electromagnetic fields, especially in closed structures like ovens. This method needs fewer computational resources as methods in the frequency domain. Broad-band calculations are easily performed. The FDTD modeling of thermal processes is also economical in memory usage. A combination with an electromagnetic FDTD leads to a very efficient and powerful simulation tool. Self-consistent modeling is possible, as well as analyzing a dynamic heating process.

Both the conductive thermal and electromagnetic algorithm are of local character as the temperature and fields in one discretization cell are only related to their neighboring cells. This local scheme applies only to conductive heat transfer. When considering radiant heat transfer, energy may be transported through the whole computational space. Mutually visible surfaces, view factors, and material parameters have to be determined and used for the calculation. This usually means high computational effort. However, the proposed method reduces this effort considerably.

The main task when including radiant heat transfer is to determine surface pairs that are mutually visible and exchanging radiant energy. A very fast algorithm has been developed that is optimized for detecting mutually visible surfaces in a rectangular nonuniform grid. This algorithm determines surface pairs very quickly. They need to be allocated and stored only once before the calculation starts. Based on this initial step, the calculation of the resulting temperature at each time step is very fast and easy.

After discussing the mechanism and modeling of the conductive and radiant heat transfer, an efficient algorithm for the computation of view factors and transfer rays is presented. The inclusion of the electromagnetic simulation is then shown. A hybrid oven simulation verifies the applicability of the method.

II. THERMAL MODELING

The first sentence of thermodynamics states that if temperature varies within a closed environment, energy has to be transported over the borders of that environment. This is expressed by

$$\rho c_{\mathrm{s}} \frac{\partial T}{\partial t} = -\mathrm{div}\, \vec{p} \qquad (1)$$

Manuscript received October 28, 2000.

J. Haala is with Marconi Communications Software Systems, D-71522 Backnang, Germany (e-mail: J.Haala@ieee.org).

W. Wiesbeck is with the Insitut für Höchstfrequenztechnik und Elektronik, Universität Karlsruhe (TH), D-76128 Karlsruhe, Germany (e-mail: Werner.Wiesbeck@etec.uni-karlsruhe.de).

Publisher Item Identifier S 0018-9480(02)04056-5.

where ρ is the density of a material, c_s is the specific heat capacity, and $\vec{p}$ is the power density, sometimes called heat flux. The right-hand side of (1) is the power that is transported in or out of an environment and that causes a temperature change.

When using a finite-difference algorithm for heat simulations [13], the structure is divided into cells that are assumed to have a constant temperature within. If (1) is applied to the volume V of the discretization cell (i, j, k) with dimensions Δx, Δy, Δz, one obtains

$$\iiint\limits_V \rho c_\mathrm{s} \frac{\partial T}{\partial t}\, dV \approx \rho c_\mathrm{s} \frac{\partial T}{\partial t} V = \rho c_\mathrm{s} \frac{\partial T}{\partial t} \Delta x\, \Delta y\, \Delta z \tag{2}$$

for the left-hand side of (1). The right-hand side becomes

$$\iiint\limits_V -\mathrm{div}\, \vec{p}\, dV = -\oiint\limits_S \vec{p} \cdot d\vec{S} = P \tag{3}$$

where P is the power that is transported into the cell and finally

$$T^{n+1}(i, j, k) = T^n(i, j, k) + \frac{\Delta t}{\rho c_\mathrm{s}\, \Delta x\, \Delta y\, \Delta z} P \tag{4}$$

is obtained if the partial derivative is replaced by

$$\frac{\partial T}{\partial t} = \frac{T^{n+1} - T^n}{\Delta t}. \tag{5}$$

The power P may be transported by: 1) heat conduction; 2) heat radiation; or 3) heat convection.

A. Conductive Heat Transfer

The power density p_c transported by heat conduction is calculated by Fourier's law

$$\vec{p}_\mathrm{c} = -\sigma_\mathrm{c}\, \mathrm{grad}\, T \tag{6}$$

where σ_c is the thermal conductivity. Applying (6) to the finite-difference scheme shown in Fig. 1, one has to calculate the power that is transported through each of the six surfaces separately. Fig. 2 shows the power

$$P_{\mathrm{c},z} = \iint\limits_A p_{\mathrm{c},z}\, dA \tag{7}$$

that is tranpsorted between two cells via their common boundary $A = \Delta x\, \Delta y$. The power $P_{\mathrm{c},z}(i, j, k)$ that is exchanged between the two cells is calculated by

$$\begin{aligned} P_{\mathrm{c},z}(i, j, k) &= -\frac{\sigma_\mathrm{c}(i, j, k-1)\sigma_\mathrm{c}(i, j, k)\, \Delta x\, \Delta y}{\frac{\Delta z(k-1)}{2}\sigma_\mathrm{c}(i, j, k) + \frac{\Delta z(k)}{2}\sigma_\mathrm{c}(i, j, k-1)} \\ &\quad \cdot \big(T(i, j, k) - T(i, j, k-1)\big) \end{aligned} \tag{8}$$

where each cell may have a different heat conductivity. However, the thermal conductivity is assumed to be constant over the volume of one discretization cell.

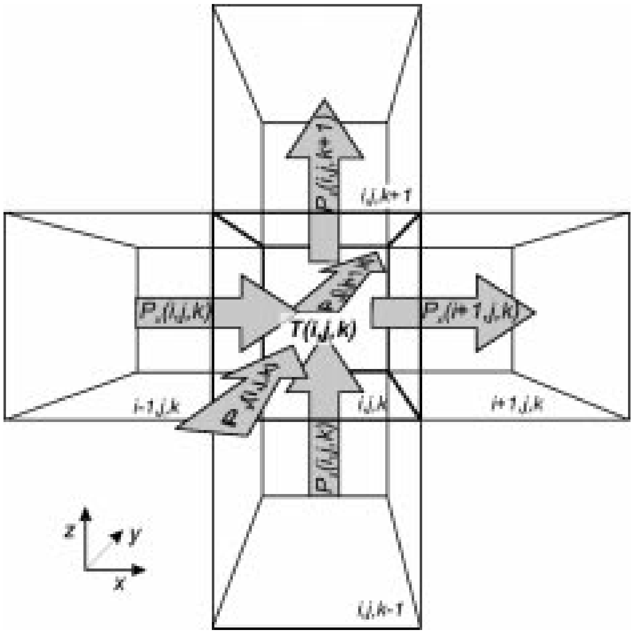

Fig. 1. Discretization cell (i, j, k) and the position of the scalar field component $T(i, j, k)$ and power vectors.

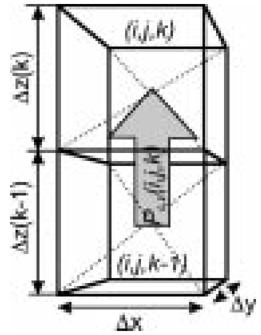

Fig. 2. Heat flux between two cells.

B. Radiant Heat Transfer

1) Theory: Heat exchange by means of heat radiation is different from heat conduction. Heat radiation does not need a medium. It only applies to surfaces. To simplify the model, all surfaces are assumed to be "gray," which means their characteristic is similar to a "black radiator," except that they do not emit or absorb all thermal radiation, but a part of it. In addition, all surfaces are assumed to radiate diffuse.

As only closed structures like ovens are considered, all radiation emitted by a surface is absorbed by another surface. The power transported between the two surfaces (Fig. 3) A_i and A_j is determined by

$$P_{i\to j,\,\mathrm{rad}} = \varepsilon_{i,\,\mathrm{rad}} A_i F_{ij} \alpha_{j,\,\mathrm{rad}} k_\mathrm{B} T_i^4 \tag{9}$$

where A_i is the size of the surface, $\varepsilon_{i,\,\mathrm{rad}}$, $\alpha_{j,\,\mathrm{rad}}$ is the part that is emitted or absorbed from A_i, and A_j, k_B is the Stefan–Boltzmann constant and T_i is the temperature of A_i. F_{ij} is called the view factor and expresses the part of energy that is transmitted by surface A_i and actually received by surface A_j, divided by the total energy emitted by surface A_i. The view factors F_{ij} are given by

$$F_{ij} = \frac{1}{\pi A_i} \int_{A_i} \int_{A_j} \frac{\cos\varphi_i \cos\varphi_j}{r^2}\, dA_j\, dA_i \tag{10}$$

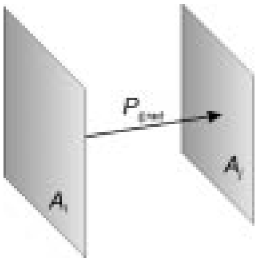

Fig. 3. Power exchanged between two surfaces.

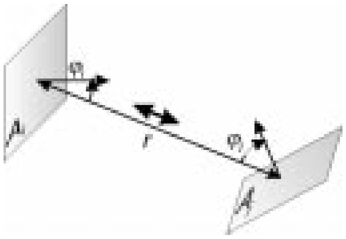

Fig. 4. Determination of the view factor F_{ij} for two surfaces A_i and A_j.

and are determined by geometrical properties, as shown in Fig. 4. The factors have values between zero for infinitesimal small surfaces infinitely separated and one for two parallel infinitely extended planes. The F_{ij} are constant with respect to temperature, and determine the part of the power that reaches A_j. It is only determined by the geometry.

The net power transmission between the two surfaces in which the opposed radiation from A_j to A_i is also considered is calculated by

$$P_{ij,\,\mathrm{rad}} = \varepsilon_{i,\,\mathrm{rad}}\varepsilon_{j,\,\mathrm{rad}}A_iF_{ij}k_{\mathrm{B}}\left(T_i^4 - T_j^4\right) \tag{11}$$

with

$$A_iF_{ij} = A_jF_{ji} \tag{12}$$

and

$$\varepsilon_{\mathrm{rad}} = \alpha_{\mathrm{rad}} \tag{13}$$

which can be proven by Kirchhoff's law.

The final temperature distribution is determined by the energy exchange between all surfaces. The radiant power flowing through the surfaces of cell $(i,\,j,\,k)$ is now used to calculate the variation of the temperature. When applying the conservation of energy (1) to the radiant heat transfer, one finally obtains

$$T^{n+1}(i,\,j,\,k) = T^n(i,\,j,\,k) + \frac{\Delta t}{\Delta x\,\Delta y\,\Delta z c_{\mathrm{s}}(i,\,j,\,k)\rho(i,\,j,\,k)} \sum_{\mathrm{Surface}} P_{\mathrm{rad}}. \tag{14}$$

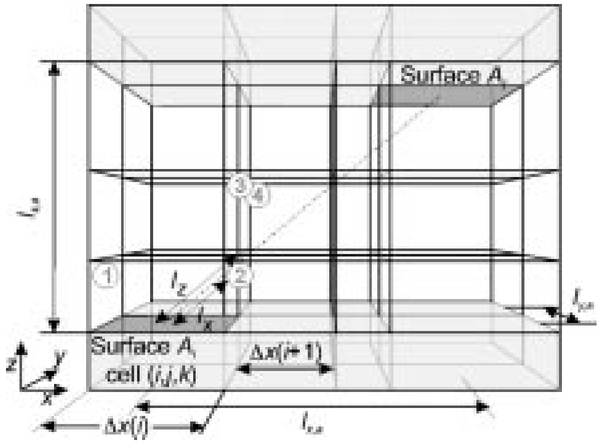

Fig. 5. Three-dimensional Bresenham algorithm in a nonuniform rectangular grid.

2) Implementation: For maximum versatility, the simulations are based on a Cartesian, but nonuniform grid. This allows an enormous simplification for the determination of view factors. An efficient calculation is obtained if the geometrical properties are checked and the view factors are calculated and stored only once before the calculation starts. During the calculation, the stored values are simply processed in a lookup table.

The preprocessing is divided into two steps. First, the relevant cells are determined. Only cells representing solid materials bordered by a gas or vacuum are relevant, as only those cells radiate or absorb energy.

The next step is to determine surface pairs. Two surfaces are called a surface pair when they exchange energy. Energy exchanges only apply to surfaces that are mutually visible. Every possible combination of surfaces has to be checked whether they are linked by a line of sight. Depending on the size and properties of the oven and the discretization, millions of possible surface pairs exist. Hence, the visibility check has to be very efficient.

Here, a modified Bresenham algorithm is used, which combines versatility and efficiency. Computer graphics use Bresenham algorithms [14], [15] to draw lines on a screen. This algorithm determines very quickly the pixels that are penetrated by a line. However, this algorithm has been developed for two-dimensional uniform grids. Here, the algorithm is extended to three-dimensional nonuniform grids. Fig. 5 shows two surfaces that are checked and whether they are mutually visible. A virtual line connects the surface centers. If each cell penetrated by the connecting line is gaseous, then the surfaces are mutually visible.

The check starts from one surface and proceeds along the connecting line. The first penetrated cell is the one directly attached to the surface. To determine which cell is penetrated next, the distances l_x, l_y, and l_z in Fig. 5 are calculated. These are the distances along the connecting line until a new cell in the x-, y-, or z-direction is reached. The distance l_x is calculated by

$$l_x = \Delta x\sqrt{1 + \frac{l_{y,\,a}^2 + l_{z,\,a}^2}{l_{x,\,a}^2}} \tag{15}$$

where Δx is the minimum distance in the x-direction to the next cell. Δx is normally the cell width and, therefore, is easily accessible. l_{xa}, l_{ya}, and l_{za} are the overall distances between the surface centers in the x-, y-, and z-direction, respectively. l_y and l_z are also calculated according to (15).

The minimum of l_x, l_y, and l_z determines whether the next penetrated cell is in the x-, y-, or z-direction. In the example in Fig. 5, the next cell is reached in the x-direction. This cell is tested if it is still gaseous. l_x is then increased by

$$l_x = l_x + \Delta x \sqrt{1 + \frac{l_{y,a}^2 + l_{z,a}^2}{l_{x,a}^2}} \qquad (16)$$

where Δx is the new cell width. The square-root term on the right-hand side is constant and is calculated only once. In comparison to the original algorithm, only one additional multiplication of the term in the square root with the actual cell width Δx is needed. This is due to the nonuniformity of the grid.

The determination of the penetrated cells is continued until a cell with solid material or the second surface A_j is reached. In the first case, the surfaces are not mutually visible.

The algorithm only determines whether there is a line of sight or not. Partial visibility is not considered since the computational effort would be very high. However, as the discretized surfaces are very small, only a slight error arises.

For each surface pair, the view factors F_{ij} are calculated. Using the reciprocity [see (12)], the view factors are calculated only once for each surface pair. As the surfaces are oriented either parallel or perpendicular in the rectangular grid, the integrals in (10) can be simplified. Reference [16] shows a method for evaluating the view factor without integration, making the calculation much faster.

C. Verification

As heat radiation is not easily separated from other heat-transfer mechanisms in practical experiments, two verifications are presented in this paper.

1) Theoretical Verification: To ensure that the numerical algorithm for the heat radiation produces accurate results, a theoretical experiment has been performed in which only heat radiation is considered. Two parallel plates exchange heat by radiation. Each plate is 100 × 100 mm and is 10-mm thick. They are separated by 200 mm (see Fig. 6). One plate has a constant temperature T_1 of 1000 K (plate 1). The other plate (plate 2) has a temperature T_2 of 0 K a the beginning and is heated by heat radiation transmitted from the other plate. It is assumed that the plates have a very high heat conductivity so that the temperature within the plates is homogeneous.

By integrating (1) over the volume V_2 of plate 2 and assuming that only heat from plate 1 may reach plate 2, one obtains

$$V_2 c_\mathrm{s} \rho \frac{\partial T_2}{\partial t} = \varepsilon_\mathrm{rad} \alpha_\mathrm{rad} F_{12} A_1 k_\mathrm{B} \left(T_1^4 - T_2^4\right). \qquad (17)$$

This equation determines the temperature T_2 at time t, which is compared to numerical simulations. One cannot explicitly solve (17), but by means of zero finding, it is possible to calculate T_2 for given time t.

For the simulation, a discretization width of 10 mm is used. This leads to 10 000 mutual visible surface pairs. The time step was chosen near the stability limit. In Fig. 7, one can see both of the results for the theoretical solution of the differential equation in comparison to the numerical simulation. The relative error

$$E = \frac{T_\mathrm{theo} - T_\mathrm{sim}}{T_\mathrm{theo}}, \qquad [T] = \mathrm{K} \qquad (18)$$

is smaller than 0.72%.

2) Measurements: To show the validity of the proposed modeling technique, a measurement setup was chosen not only to verify heat radiation, but the complete model. As shown in Fig. 8, a heating plate was used to heat up a block of aluminum. The heating plate has a sensor within and one is able to assure a constant temperature of the plate by means of a control unit. Therefore, the temperature of the plate was assumed to be constant. A block of aluminum was heated on the plate. In the middle of the block, temperature sensitive paper was placed

Fig. 6. Two parallel plates exchanging heat by radiation.

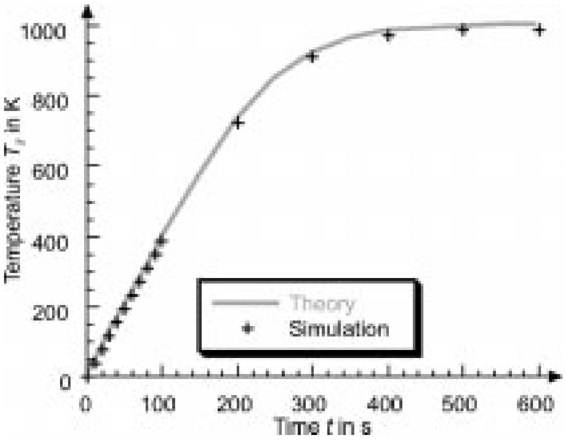

Fig. 7. Comparison between theoretical and simulated result.

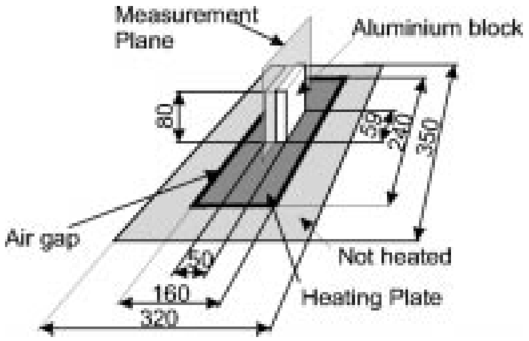

Fig. 8. Measurement setup for the validation of the heat modeling. All dimensions are in millimeters.

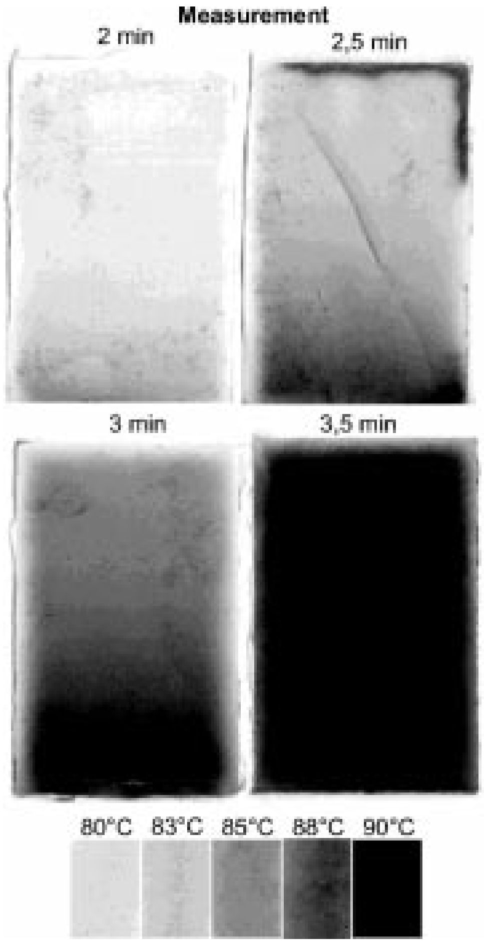

Fig. 9. Measurement results for different heating times of the aluminum block. The shadings of the thermosensitive paper were determined using the temperature-controlled heating plate.

to measure the heat distribution within the block. The paper changes its color from white to black within the temperature range from 80 °C to 90 °C. The color of the paper depends not on the time exposed to the temperature, but only on the temperature itself. The shadings of the thermosensitive paper were determined using the temperature-controlled heating plate.

The heating plate has a constant temperature of 110 °C, while the aluminum block has a temperature of 20 °C at the beginning of the measurement. In Fig. 9, the resulting temperature distributions are shown for different heating times of the aluminum block.

The simulations were performed using the material parameters given in Table I, which were taken from [17]. To ease the comparison of measured and simulated results, a similar color distribution was used to print the simulation results. As shown in Fig. 10, there is a very good agreement between simulated and measured results. The relative error

$$E = \frac{T_{\text{theo}} - T_{\text{sim}}}{T_{\text{theo}}}, \qquad [T] = \text{K} \tag{19}$$

is smaller than 1%.

TABLE I
MATERIAL PARAMETERS USED IN THE SIMULATION

parameter	value	T in K
aluminium		
spec. heat capacity in J/K kg	903	300
	949	400
density in kg/m^3	2702	300–400
therm. conductivity in W/m K	237	300
	240	400
emission coefficient	0.9	300-400
air		
spec. heat capacity in J/K kg	1009	270
	1005	300
	1007	350
	1008	370
density in kg/m^3	1.311	270
	1.177	300
	1.012	350
	1.0956	370
therm. conductivity in W/m K	0.0249	270
	0.0267	300
	0.0300	350
	0.0313	370

III. MICROWAVE HEATING

The heating of materials with microwaves is determined directly by

$$P_{\text{elec}} - \iiint_V c_{\text{s}}(\vec{x}, T)\rho(\vec{x}, T)\,\frac{\partial}{\partial t}\,T(\vec{x}, T)\,dV = 0 \tag{20}$$

where P_{elec} is the microwave power dissipated. As shown in Fig. 11, there are 12 electric-field components dissipating power within one cell. The electromagnetic power

$$P_{\text{elec}} = \frac{\Delta x\,\Delta y\,\Delta z}{4}\sum_{n=1}^{12}\kappa|E_n|^2 \tag{21}$$

is determined by the electric conductivity κ of the material. Combining (20) and (21) and setting up the finite-difference scheme, one obtains

$$\begin{aligned} &T^{n+1}(i, j, k) \\ &\quad = T^n(i, j, k) + \frac{\Delta t}{4c_{\text{s}}(i, j, k)\rho(i, j, k)}\sum_{n=1}^{12}\kappa|E_n|^2. \end{aligned} \tag{22}$$

The computation of the electric energy dissipated in one cell is done by a standard FDTD scheme, and includes linear and frequency-dependent materials.

Additionally, (4), (8), (14), and (22) are combined to update the temperature in only one computational step. The radiant, conductive, and electric power is summed up leading to

$$\begin{aligned} &T^{n+1}(i, j, k) \\ &\quad = T^n(i, j, k) + \frac{\Delta t}{\Delta x\,\Delta y\,\Delta z c_v(i, j, k)\rho(i, j, k)} \\ &\qquad \cdot \left(\sum_{\text{Surface}} P_{\text{rad}} + \sum_{\text{Surface}} P_{\text{c}} + \sum_{\text{Volume}} P_{\text{elec}}\right). \end{aligned} \tag{23}$$

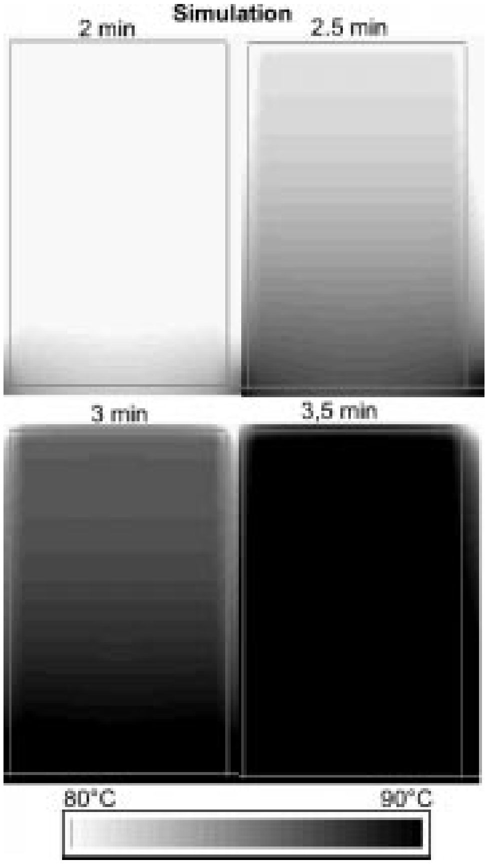

Fig. 10. Simulated temperature distribution within the aluminum block after different heating times.

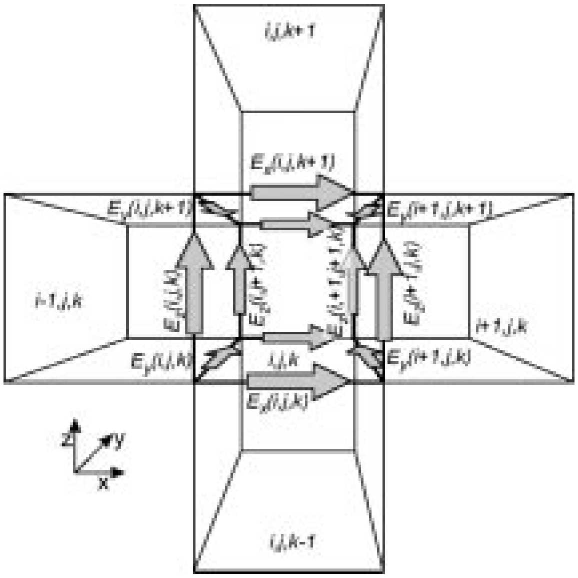

Fig. 11. Placement of the electric-field components within the discretization cell $(i,\ j,\ k)$.

IV. SIMULATION OF A HYBRID OVEN

In this section, the above method is applied to the simulation of a hybrid oven loaded with material samples. The oven has the dimensions of $400 \times 360 \times 350\ \mathrm{mm}^3$ and is sketched in Fig. 12. The placement of the samples is sketched in Fig. 13.

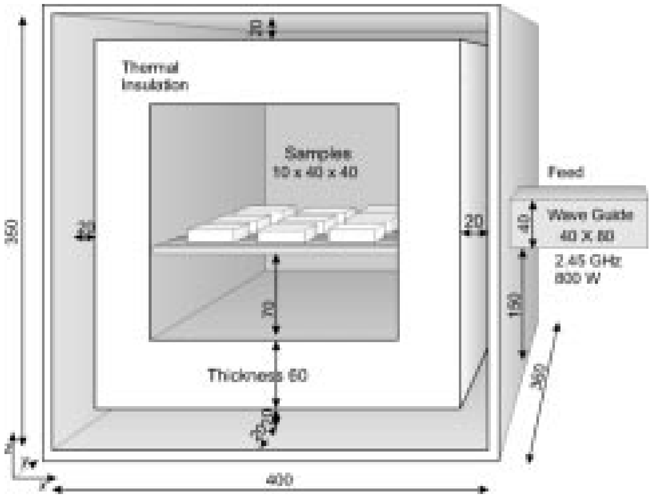

Fig. 12. Hybrid oven with casket and samples inside. The samples are placed on bars. The front, rear, top, and bottom walls are heated conventionally. Dimensions are in millimeters.

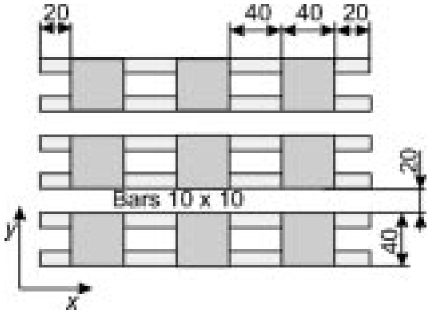

Fig. 13. Placement of the samples on the bars. Dimensions are in millimeters.

The walls of the oven consist of carbon. Inside the oven, an Al_2O_3 casket carries four samples on Al_2O_3 bars. The electromagnetic and thermal material parameters of the casket and the samples are summarized in Table II.

A. Characterization of Thermal and Electromagnetic Field Distribution

To get more detailed information on the temperature and electromagnetic field distribution within the samples, two statistical values are defined. The first one is the *homogeneity*

$$\mathrm{HO}_{\mathrm{elec}} = \frac{E[|E|^2]}{\sigma_{|E|^2}} \tag{24}$$

$$\mathrm{HO}_{\mathrm{therm}} = \frac{E[T]}{\sigma_T} \tag{25}$$

where $E[F()]$ is the expectation value of function $F()$, and $\sigma_{F()}$ is the corresponding standard deviation. At the beginning of a simulation, the homogeneity of the temperature distribution $\mathrm{HO}_{\mathrm{therm}}$ is infinite since the structure has thermal equilibrium, and the standard deviation is zero. Equations (24) and (25) allow to characterize both the thermal and electromagnetic field distribution. To obtain information about local maxima

TABLE II
MATERIAL PARAMETERS USED IN THE SIMULATION

material	parameter	value	T in K
samples	spec. heat cap. c_v	765	300
		940	400
		1110	600
	density ρ	3970	0-1000
	thermal cond. σ	36	300
		27	400
		16	600
		10	1000
	emission-,	0.78	400
	abs.-coeff.	0.69	600
	$\varepsilon = \alpha$	0.61	800
		0.51	1000
	rel. perm. $\varepsilon_{\mathrm{el}}$	9.6	0-1000
	el. cond. κ	0.05	0-1000
casket + bars	same as samples except		
	el. cond. κ	0.01	0-1000

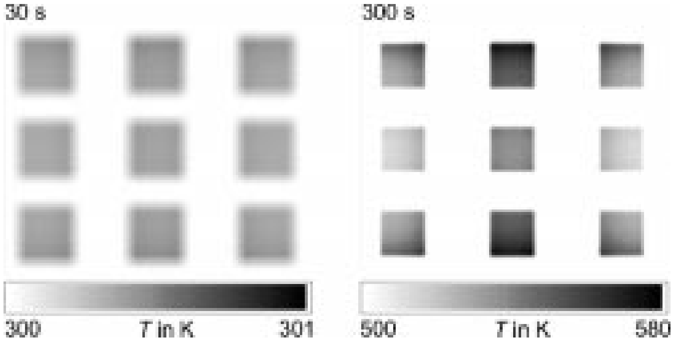

Fig. 14. Temperatures T for the conventional heating at time steps $t = 30$ s and $t = 300$ s for a view plane at $x = 165$ mm. Resulting characteristic values: $\mathrm{HO}(t = 30\ \mathrm{s}) \to \infty$, $\mathrm{HO}(t = 300\ \mathrm{s}) = 35.26$, $\mathrm{HSF}(t = 30\ \mathrm{s}) = 0.0$, $\mathrm{HSF}(t = 300\ \mathrm{s}) = 0.06$.

or minima that do not have significant influence on the homogeneity, an additional parameter is defined for characterization, i.e., the *hot-spot factor*

$$\mathrm{HSF}_{\mathrm{elec}} = \frac{\mathrm{Max}\{|E^2 - E[|E|^2]|\}}{E[|E|^2]} \tag{26}$$

$$\mathrm{HSF}_{\mathrm{therm}} = \frac{\mathrm{Max}\{T - E[T]\}}{E[T]} \tag{27}$$

detects local extrema within in the field distribution. Again, the same formulation is used for both the thermal and electromagnetic field distribution.

B. Conventional Heating

The front and rear walls of the oven are heated with a constant rate of 5 K/s. The insulation shown in Fig. 12 is not used in this configuration. Computational results are given in Fig. 14 for $t = 30$ s and $t = 300$ s. The homogeneity is $\mathrm{HO}(t = 30\ \mathrm{s}) \to \infty$ and $\mathrm{HO}(t = 300\ \mathrm{s}) = 35.26$. The hot-spot factor is $\mathrm{HSF}(t = 30\ \mathrm{s}) = 0.0$ and $\mathrm{HSF}(t = 300\ \mathrm{s}) = 0.06$. The samples are not heated within the first 30 s, as the walls are not hot enough to transfer much heat radiation to the samples. As the samples are not heated, there is still thermal equilibrium and a very high homogeneity. After 300 s, the samples are heated up by 200 K. As radiation transports the heat to the samples and the samples shadow each other, temperature gradients arise. The scales in the figures are adjusted to the maximum temperature reached.

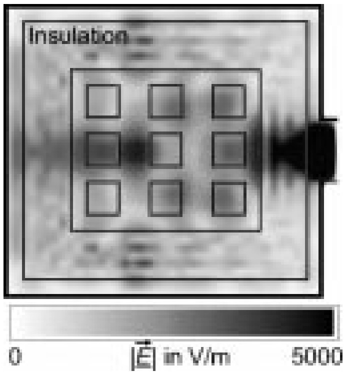

Fig. 15. Electric-field strength $|E|$ within the oven for a view plane at $x = 165$ mm at $f = 2.45$ GHz. Resulting characteristic values: $\mathrm{HO} = 1.25$, $\mathrm{HSF} = 1.07$.

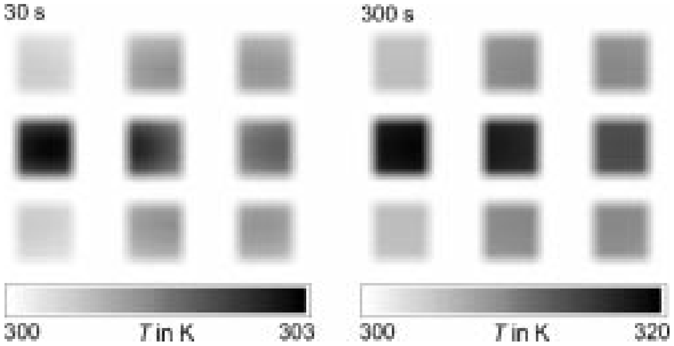

Fig. 16. Temperatures T for the microwave heating at time steps $t = 30$ s and $t = 300$ s for a view plane at $x = 165$ mm. Resulting characteristic values: $\mathrm{HO}(t = 30\ \mathrm{s}) = 440$, $\mathrm{HO}(t = 300\ \mathrm{s}) = 67.17$, $\mathrm{HSF}(t = 30\ \mathrm{s}) = 0.007$, $\mathrm{HSF}(t = 300\ \mathrm{s}) = 0.29$.

For faster heating, one has to increase the heating rate of the walls. However, this would cause stronger temperature gradients. For a faster and more homogeneous heating at the same time, one has to use different heat sources.

C. Microwave Heating

In this configuration, the oven is only heated by microwaves. To avoid strong temperature gradients due to the different temperatures of the hot samples and cold walls, a thermal insulation (see Fig. 12) is used. The microwave power is fed through a waveguide with dimensions 80 × 40 mm^2 located in the middle of a sidewall. The generator has a frequency of 2.45 GHz and produces 800-W microwave power. In Fig. 15, the electromagnetic field distribution at $f = 2.45$ GHz in the frequency domain is given in a view plane at $x = 165$ mm. Clearly seen are the resonances arising within the casket.

In Fig. 16, the temperature distribution is given for 30 and 300 s. The samples near the microwave feed are heated faster.

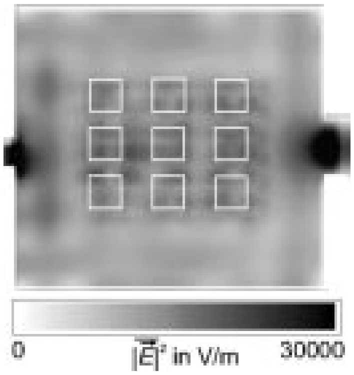

Fig. 17. Electric-field strength within the oven for a view plane at $x = 165$ mm. The field is generated by two broad-band (500 MHz) generators at $f = 2.45$ GHz center frequency. Resulting characteristic values: $\mathrm{HO} = 2.50, \mathrm{HSF} = 0.66$.

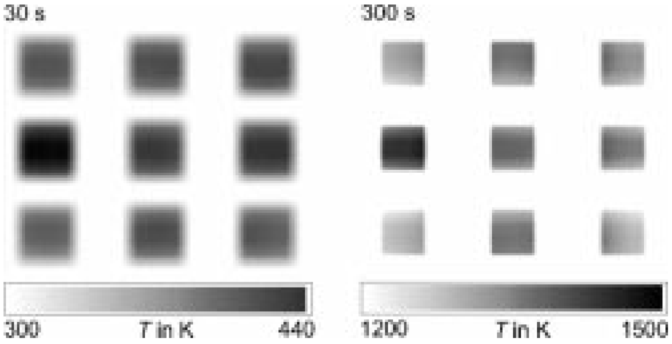

Fig. 18. Temperatures T for the hybrid heating at $t = 30$ s and $t = 300$ s for a view plane at $x = 165$ mm. Resulting characteristic values: $\mathrm{HO}(t = 30\ \mathrm{s}) = 23.6, \mathrm{HO}(t = 300\ \mathrm{s}) = 26.6, \mathrm{HSF}(t = 30\ \mathrm{s}) = 0.12, \mathrm{HSF}(t = 300\ \mathrm{s}) = 0.11$.

One can see that the median temperature after 300 s is only approximately 15 K higher than at the beginning. The problem is that not only the samples are heated by the microwaves, but also the insulation. To increase the heating rate, one has to increase the microwave power. However, in this paper, another solution is presented that allows the increase of the heating rate by a combination with the conventional heating previously shown.

D. Hybrid Heating

To achieve a fast and uniform heating, the microwave and conventional heating are combined. This allows removal of the thermal insulation from the oven. Simulations of a simple combination of both heating sources show a fast heating. However, due to the resonance in the electromagnetic field, the temperature distribution is not homogenous.

To achieve a good homogeneity within the oven, broad-band microwave generators are used. Fig. 17 shows the electromagnetic field distribution with two broad-band generators, each fed into the oven by a waveguide. The waveguides are mounted on opposite sides of the oven and have an orthogonal polarization. The bandwidth of the generators is 500 MHz and each one produces 800-W microwave power. The field distribution shows an excellent homogeneity.

The results for the temperature distribution after 30 and 300 s are shown in Fig. 18. One can see that a rapid and homogeneous heating is achieved by the combination of the two heat sources. As the electromagnetic field distribution is homogeneous, the heating of the samples is also homogeneous. The mean temperature of the samples after 300 s is significantly higher than the resulting temperature of the conventional or microwave heating alone.

This example shows that the combination of different heat sources offers the opportunity for a fast and homogeneous heating. However, the electromagnetic field distribution has a great influence on the homogeneity of the temperature. Conventional heating via heated oven walls only influences the temperature near the surface of the samples. The best results are achieved if both sources are adjusted to each other so that the oven walls have nearly the same temperature as the samples.

V. CONCLUSION

A new method was presented to simulate heating processes including thermal energy exchanges by conduction and radiation. The algorithms are implemented within an electromagnetic FDTD code, allowing the calculation of conventionally and microwave heated ovens. For the conductive heat transfer, a finite-difference scheme is used. Ray optical methods are introduced to check visibility of surfaces and, consequently, the radiant heat exchange. The resulting simulation tool is very powerful and mandatory for the design of high-quality ovens. It allows the determination of temperature distribution inside materials and an optimization for any desired heat pattern. Especially for hybrid ovens where different heat sources have to be adjusted, the developed software package has proven to offer an excellent opportunity to simulate heating processes and to support hybrid oven designs. For the verification of the results, two new definitions, i.e., homogeneity and hot-spot factor, are introduced.

REFERENCES

[1] T. V. Chow Ting Chan and H. C. Reader, "Modeling of modes and perspectives on multiple-feeds in microwave ovens," *J. Microw. Power Electromagn. Energy*, vol. 31, no. 4, pp. 238–250, 1996.

[2] W. Fu and A. Metaxas, "Numerical prediction of three-dimensional power density distribution in a multi-mode cavity," *J. Microw. Power Electromagn. Energy*, vol. 29, no. 2, pp. 67–75, 1994.

[3] M. F. Iskander, R. L. Smith, A. Octavio, M. Andrade, H. Kimrey, and L. M. Walsh, "FDTD simulation of microwave sintering of ceramics in multimode cavities," *IEEE Trans. Microwave Theory Tech.*, vol. 42, pp. 793–800, May 1994.

[4] K. Iwabuchi, T. Kubota, and T. Kashiwa, "Analysis of electromagnetic fields in a mass-produced microwave oven using the finite-difference time-domain method," *J. Microw. Power Electromagn. Energy*, vol. 31, no. 3, pp. 188–196, 1996.

[5] G. A. Kriegsmann, "Cavity effects in microwave heating of ceramics," *Siam J. Appl. Math.*, vol. 57, pp. 382–400, Apr. 1997.

[6] F. Liu, I. Turne, and M. Bialkowski, "A finite-difference time-domain simulation of power density distribution in a dielectric loaded microwave cavity," *J. Microw. Power Electromagn. Energy*, vol. 29, no. 3, pp. 138–148, 1994.

[7] M. Subirats, M. F. Iskander, M. J. White, and J. O. Kiggans, Jr., "FDTD simulation of microwave sintering in large (500/4000 liter) multimode cavities," *J. Microw. Power Electromagn. Energy*, vol. 32, no. 3, pp. 161–170, 1997.

[8] S. Sundberg, P. Kildal, and T. Ohlsson, "'Moment method analysis of a microwave tunnel oven," *J. Microw. Power Electromagn. Energy*, vol. 33, no. 1, pp. 36–48, 1998.

[9] H. Zhao and I. W. Turner, "An analysis of the finite-difference time-domain method for modeling the microwave heating of dielectric materials within a three-dimensional cavity system," *J. Microw. Power Electromagn. Energy*, vol. 31, no. 4, pp. 199–214, 1996.

[10] ——, "A generalized finite-volume time-domain algorithm for microwave heating problems on arbitrary irregular grids," in *13th Annu. Rev. Progress Appl. Comput. Electromagn.*, vol. 31, Mar. 1996, pp. 199–214.

[11] F. Torres and B. Jecko, "Complete FDTD analysis of microwave heating processes in frequency-dependent and temperature-dependent media," *IEEE Trans. Microwave Theory Tech.*, vol. 45, pp. 108–117, Jan. 1997.

[12] L. Ma, D.-L. Paul, N. Pothecary, C. Railton, J. Bows, L. Barratt, J. Mullin, and D. Simons, "Experimental validation of a combined electromagnetic and thermal FDTD model of a microwave heating process," *IEEE Trans. Microwave Theory Tech.*, vol. 43, pp. 2565–2571, Nov. 1995.

[13] M. Shashkow, *Conservative Finite-Difference Methods on General Grids*. Boca Raton, FL: CRC Press, 1996.

[14] B. Zalik, G. Clapworthy, and C. Oblonsek, "An efficient code-based voxel-traversing algorithm," *Comput. Graph. Forum*, vol. 16, pp. 119–147, June 1997.

[15] C. Yuesheng and C. Zhenchu, "The Bresenham's line algorithm in multidimension," in *Proc. 4th Int. Computer-Aided Drafting, Design, Manufact. Technol. Conf.*, Aug. 1994, pp. 133–139.

[16] C. Hsu, "Shape factor equations for radiant heat transfer between two arbitrary sizes of rectangular planes," *Can. J. Chem. Eng.*, vol. 45, pp. 115–120, 1967.

[17] A. F. Mills, *Heat Transfer*. Englewood Cliffs, NJ: Prentice-Hall, 1999.

Jens Haala (S'96–M'01) was born in Heilbronn, Germany, in 1970. He received the Dipl.-Ing. (M.S.E.E.) and Dr.-Ing. (Ph.D.E.E.) degrees from the Universität Karlsruhe (TH), Karlsruhe, Germany, in 1996 and 2000, respectively.

From 1996 to 2001, he was a Research Assistant with the Institut für Höchstfrequenztechnik und Elektronik (IHE), Universität Karlsruhe (TH). Since January 2001, he has been with Marconi Communications Software Systems, Backnang, Germany. His research interests include electromagnetic compatibility, microwave heating, and material measurements, as well as numerical modeling of electromagnetic wave propagation and microwave heating.

Werner Wiesbeck (SM'87–F'94) received the Dipl.-Ing. (M.S.E.E.) and Dr.-Ing. (Ph.D.E.E.) degrees from the Technical University of Munich, Munich, Germany, in 1969 and 1972, respectively.

From 1972 to 1983, he held various positions with AEG-Telefunken, including that of Head of Research and Development of the Microwave Division, Flensburg, Germany, and Marketing Director of the Receiver and Direction Finder Division, Ulm, Germany. During this time, he had product responsibility for millimeter-wave radars, receivers, direction finders, and electronic-warfare systems. Since 1983, he has been Director of the Institut für Höchstfrequenztechnik und Elektronik (IHE), Universität Karlsruhe (TH), Karlsruhe, Germany. His research interests include radar, remote sensing, wave propagation, and antennas. In 1989 and 1994, respectively, he spent a six-month sabbatical with the Jet Propulsion Laboratory, Pasadena, CA. For the Carl Cranz Series for Scientific Education, he serves as a permanent Lecturer for "Radar System Engineering" and "Wave Propagation."

Dr. Wiesbeck is a member of an Advisory Committee of the European Union (EU) Joint Research Centre (Ispra/Italy). He was a member of the IEEE Geoscience and Remote Sensing Society (IEEE GRS-S) Administrative Committee (AdCom) (1992–2000), chairman of the IEEE GRS-S Awards Committee (1994–1998), executive vice president of the IEEE GRS-S (1998–1999), president of the IEEE GRS-S (2000–2001), associate editor of the IEEE TRANSACTIONS ON ANTENNAS AND PROPAGATION (1996–1999), and past treasurer of the IEEE German Section. He was general chairman of the 1988 Heinrich Hertz Centennial Symposium, the 1993 Conference on Microwaves and Optics (MIOP'93), and he has been a member of scientific committees of numerous conferences. He is an advisor to the German Research Council (DFG), the Federal German Ministry for Research (BMBF), and to industry in Germany.